

1 Surface cooling linked to increased glacial carbon storage via
2 changes in Antarctic sea ice

3 Alice Marzocchi¹ and Malte F Jansen²

4 ¹National Oceanography Centre, Southampton, SO14 3ZH (UK)

5 ²Dept. of the Geophysical Sciences, The University of Chicago, Chicago, IL 60637 (USA)

6 **Paleoceanographic reconstructions indicate that the distribution of global**
7 **ocean water masses has undergone major glacial-interglacial rearrangements**
8 **over the past ~2.5 million years. Given that the ocean is the largest carbon**
9 **reservoir, such circulation changes were likely key in driving the variations**
10 **in atmospheric CO₂ concentrations observed in the ice-core record. However,**
11 **we still lack a mechanistic understanding of the ocean's role in regulating**
12 **CO₂ on these time scales. Here we show that glacial ocean-sea-ice numeri-**
13 **cal simulations with a single-basin general circulation model, forced solely by**
14 **atmospheric cooling, can predict ocean circulation patterns associated with**
15 **increased atmospheric carbon sequestration in the deep ocean. Under such**
16 **conditions, Antarctic Bottom Water becomes more isolated from the sea sur-**
17 **face as a result of two connected factors: reduced air-sea gas exchange under**

18 sea ice around Antarctica and weaker mixing with North Atlantic Deep Wa-
19 ter due to a shallower interface between southern and northern-sourced water
20 masses. These physical changes alone are sufficient to explain ~ 40 ppm atmo-
21 spheric CO_2 drawdown; about half of the glacial-interglacial variation. Our
22 results highlight that atmospheric cooling could have directly caused the reor-
23 ganization of deep ocean water masses and, thus, glacial CO_2 drawdown. This
24 provides an important step forward towards a consistent picture of glacial
25 climates.

26 Since the onset of the Northern Hemisphere glaciation (~ 2.7 million years ago), Earth's
27 climate has undergone large transitions between cold glacial and warm interglacial (e.g.,
28 present-day) stages. The geological record suggests that such transitions were also ac-
29 companied by large-scale ocean circulation changes, which were likely key in the glacial-
30 interglacial shifts themselves, by affecting the partitioning of carbon between the atmo-
31 sphere and the ocean (1; 2).

32 The distribution of carbon, heat and freshwater throughout the global ocean is largely
33 shaped by the meridional overturning circulation, which today consists of two main over-
34 turning cells that originate in the polar regions. The upper cell, or Atlantic Meridional
35 Overturning Circulation (AMOC), is associated with sinking of dense water to depths of
36 ~ 3 km in the subpolar North Atlantic; the abyssal cell is fed by the formation of even
37 denser water around Antarctica. Antarctic Bottom Water (AABW) formation and wind-

38 driven upwelling of deep waters originating from both hemispheres make the Southern
39 Ocean the dominant conduit for the exchange of heat and carbon between the surface
40 and the abyss (3).

41 The leading interpretations of geochemical water mass tracers indicate that ocean circu-
42 lation was substantially different during the Last Glacial Maximum (LGM, ~21,000 years
43 ago) and characterized by a shallower AMOC (4; 5; 6). The glacial deep ocean was not
44 only colder, but also likely more stratified and saltier (7; 8). The interpretation of many
45 of these reconstructions is, however, still debated (9). To further complicate matters, the
46 representation of the glacial ocean state in coupled climate simulations differs substan-
47 tially between models and is often at odds with the geological evidence (10; 11; 12).

48 A number of studies have highlighted the key role of Antarctic sea ice and the result-
49 ing surface buoyancy forcing in driving the inferred glacial-interglacial rearrangements in
50 global ocean water masses (13; 14; 15; 16; 17; 18; 19; 20; 21). A recent study directly linked
51 glacial circulation changes to atmospheric cooling (18), suggesting that enhanced brine
52 rejection from Antarctic sea-ice formation in a colder climate leads to increased abyssal
53 stratification and ultimately a shoaling of the AMOC (22). Coupled climate models simu-
54 lating strong LGM sea-ice formation have also been shown to exhibit enhanced stratifica-
55 tion and a shallower AMOC, largely consistent with the geological evidence, while LGM
56 simulations with relatively little Antarctic sea ice typically reveal the opposite response
57 (12).

58 Since the ocean is the largest carbon reservoir that reacts on glacial-interglacial time-
59 scales, the suggested changes in ocean circulation may play an important role in explaining
60 the variations in atmospheric CO₂ concentrations between glacial and interglacial climates
61 (1; 2). Several modelling studies have investigated the ocean's role in glacial-interglacial
62 changes in carbon storage (23; 24; 25; 26; 27; 28; 29), but no consensus has yet been reached
63 on which are the dominant drivers and processes. The existing studies typically use models
64 with highly simplified physics, coarse resolution, and/or a complex coupling between the
65 atmosphere, sea ice and ocean components. In addition, physical and biogeochemical
66 drivers have often been considered in conjunction, which makes it difficult to disentangle
67 the response to a number of changes in the boundary conditions and to obtain a deeper
68 mechanistic understanding of the results.

69 Here we apply an idealized yet physically robust setup, using an ocean-sea-ice general
70 circulation model (GCM), where changes in the ocean circulation and biogeochemistry
71 are forced solely by atmospheric cooling (see Methods). The physical changes between a
72 warm (interglacial) and cold (glacial) climate are described in a previous manuscript (18)
73 and are broadly consistent with the available LGM proxy record. The model setup uses
74 an idealized geometry, which includes only one ocean basin, but simulations with multiple
75 ocean basins and more complex coupled climate models suggest that the idealized model
76 reproduces the global mean meridional overturning circulation changes found in multi-
77 basin models (12; 21). In this study, we also include a biogeochemical model with a closed

78 carbon cycle to gain a mechanistic understanding of the role of the physical changes in
79 regulating glacial atmospheric CO₂.

80 **Simulated glacial ocean circulation and carbon storage**

81 In our ocean-sea-ice simulations, a lowering of atmospheric temperature leads to an ex-
82 pansion of Antarctic sea-ice cover and increased deep-ocean stratification, as compared
83 to the Pre-Industrial (PI) reference simulation (Figure 1), in agreement with LGM recon-
84 structions (7; 30). The “LGM-like” ocean circulation is also characterized by a shallower
85 AMOC, further separated from the abyssal cell than in the “PI-like” case (Figure 1), again
86 broadly consistent with the paleoclimate record (5). Changes in the deep ocean circula-
87 tion and stratification have been attributed to enhanced brine rejection from Antarctic
88 sea-ice formation in a colder climate, which leads to increased abyssal stratification (18).
89 The larger abyssal stratification in turn leads to a shoaling of the AMOC (22). In the
90 LGM configuration, AABW is more isolated from the surface due to 1) weaker mixing
91 with North Atlantic Deep Water (NADW) as a result of a shoaling of the interface be-
92 tween the upper and abyssal cells to a depth where turbulent vertical mixing is reduced
93 (31; 21), and 2) reduced air-sea gas exchange under expanded sea ice around Antarctica
94 (13). The change in sea ice and circulation is, therefore, likely to favor increased carbon
95 sequestration in the glacial deep ocean.

96 We test the increased glacial carbon storage hypothesis by coupling the physical ocean-sea-

97 ice model (18) to a biogeochemistry model (32) and a well-mixed atmospheric box, which
98 allows atmospheric CO_2 concentrations to adjust while total carbon is conserved (33).
99 Under glacial conditions, the dissolved inorganic carbon (DIC) concentration increases
100 substantially in the deep ocean (Figure 2b), as a consequence of cooling, sea-ice expansion
101 and circulation changes. This results in a drawdown of atmospheric CO_2 concentrations
102 by 40 ppm from 278 ppm in the PI to 238 ppm in the LGM (Figure 2 and Table 1), which
103 corresponds to about half of the inferred glacial-interglacial variations (34).

104 To better understand the changes in the partitioning of carbon between the atmosphere
105 and ocean, we diagnostically decompose the atmospheric CO_2 drawdown into different
106 physical and biological contributions (25; 35; 36; 37). The most easily understood contri-
107 bution is associated with the solubility pump (38; 39), which reflects the dependence of
108 CO_2 solubility on the ocean's temperature and (to a lesser extent) salinity. As the ocean
109 gets colder, it can dissolve more carbon, but this only explains about 16 of the 40 ppm
110 of atmospheric pCO_2 drawdown between the PI and LGM reference simulations (Figure
111 2 and Table 1).

112 The largest contribution instead is associated with a strengthening of the disequilibrium
113 pump, which reflects the air-sea disequilibrium at the surface. The large air-sea disequilib-
114 rium in the LGM simulation results from the fact that the abyssal overturning circulation,
115 which carries waters enriched in DIC by the biological pump, reaches the surface only un-
116 der sea ice around Antarctica, where outgassing is strongly inhibited. As a result, the

117 disequilibrium pump drives a reduction of atmospheric CO₂ between the PI and LGM
118 reference simulations of 39 ppm.

119 Some of the disequilibrium pump contribution, however, is offset by a reduction in the
120 biological pump, which represents the export of carbon into the deep ocean via organic
121 matter. The apparent weakening of the biological pump and an associated enhancement
122 in the disequilibrium pump in the LGM simulation are likely related to changes in AABW
123 formation processes, and highlight some of the challenges in the interpretation of the car-
124 bon pump decomposition. In the present-day-like control simulation, convection at high
125 southern latitudes does not fully reach the surface (not shown), but instead appears to be
126 triggered by a subsurface cabelling instability (40). As a result, circumpolar deep water
127 (CDW) is transformed into AABW with little direct surface exposure (although there is
128 mixing between CDW and surface waters). Since the diagnostic carbon pump decompo-
129 sition only considers water that enters the surface model layer as ventilated, upwelling
130 phosphate is not relabeled as preformed, which leads to an apparently efficient biological
131 pump. In the LGM simulation, deep convection instead does reach to the surface, but
132 CDW mostly comes to the surface under sea ice, where it is exposed to little air-sea gas
133 exchange and relatively little biological production. However, any remineralized nutrients
134 that come to the surface (even under ice) are relabeled as preformed, thus weakening the
135 biological pump, while the associated DIC contributes to the disequilibrium pump. This
136 highlights that compensating changes in the biological and disequilibrium pump need to

137 be interpreted with caution, especially in the presence of sea ice. Nevertheless, our results
138 highlight unambiguously that changes in sea ice and circulation in the colder climate more
139 than double the CO₂ drawdown that would be expected from the solubility effect alone.

140 **Sensitivity experiments and carbon pump decomposition**

141 To illustrate the importance of Antarctic sea-ice dynamics in explaining glacial atmo-
142 spheric pCO₂ drawdown, we performed a sensitivity experiment where air-sea gas ex-
143 change and biogeochemistry do not depend on the sea ice cover (i.e. the presence of sea
144 ice is simply ignored in the computation of the air-sea flux of CO₂). The atmospheric CO₂
145 concentration in the PI simulation is virtually unaffected by this change, which may be
146 understood by noting that the abyssal cell is not as strongly isolated from the upper cell,
147 such that not as much DIC can accumulate in the first place (21). In the LGM simula-
148 tion, the CO₂ concentration instead increases from 238 (in the LGM reference) to 268 ppm
149 when the sea ice effect is removed, corresponding to a drawdown between PI and LGM
150 of only 10 ppm (Table 1). The carbon pump decomposition indicates that the difference
151 between the LGM simulation with and without sea-ice effects on air-sea gas exchange is
152 explained almost entirely by a change in the efficiency of the disequilibrium pump (see
153 Table 1). The mechanism for the drawdown of atmospheric pCO₂ here appears to differ
154 from that described in (27), which invokes a more efficient biological pump, driven by an
155 increased residence time of waters near the surface, as opposed to a disequilibrium pump

156 driven by suppressed air-sea gas exchange under sea ice in our case.

157 The important role of the disequilibrium pump is qualitatively consistent with the results
158 of (41); however, contrary to our results, these authors suggest that sea ice is not a major
159 driver of the disequilibrium pump. This may be a result of differences in the models used,
160 but it may also arise from differences in the analysis. While we estimate the role of sea ice
161 by eliminating the effect of sea ice on biogeochemistry in both PI and LGM experiments,
162 their conclusion is based on sensitivity experiments using LGM sea-ice cover in the PI
163 simulation and vice versa. Prescribing LGM sea ice with PI ocean circulation does not
164 account for the tight coupling between sea ice and circulation changes (e.g. 17; 18) and
165 limits the drawdown potential, because the decoupling of the lower and upper cells and
166 suppression of air-sea gas exchange need to act together to isolate the abyssal water masses
167 (21).

168 Estimates of LGM circulation and carbon storage are expected to be sensitive to the verti-
169 cal (i.e. diapycnal) mixing rate, whose magnitude is uncertain. The lower sea level would
170 have significantly reduced the extent of shallow shelf seas, which likely led to enhanced
171 tidal energy dissipation in the deep ocean, thus providing more energy for turbulent
172 mixing (e.g. 42; 43). At the same time, strongly enhanced deep ocean stratification, as
173 predicted by our model, means that more energy is required to maintain a similar amount
174 of vertical mixing (e.g. 44). As a result, the net change in mixing rates is uncertain. To
175 test the sensitivity of LGM ocean carbon storage to changes in the vertical mixing rates

176 in our model, we performed two sensitivity experiments where the diapycnal diffusivity
177 was increased and reduced by 50%, respectively (see Table 1). Increased diffusivity re-
178 duces carbon uptake in the LGM, which is consistent with the expectation that carbon
179 sequestration in the deep ocean is less effective in the presence of strong vertical mixing
180 (e.g. 45). Surprisingly, reduced mixing also leads to slightly reduced carbon uptake in the
181 LGM, apparently as a result of a weaker biological pump (see Table 1).

182 Changes in the disequilibrium pump instead are more robust: its contribution is increased
183 with reduced diffusivity and decreased with enhanced diffusivity (Table 1), consistent
184 with the expectation that water masses in the abyssal cell become increasingly isolated,
185 mixing less with the relatively well-ventilated water masses of the upper cell. These results
186 indicate that changes in the vertical mixing rate may have played an important role in
187 the glacial carbon cycle, although the net effect on carbon storage is complex and may be
188 sensitive to the specific magnitude and structure of vertical mixing, which are very hard
189 to predict.

190 While the focus of this study is on the physical drivers of ocean carbon storage associated
191 directly with atmospheric cooling, it has often been suggested that changes in biological
192 productivity, driven e.g. by changes in temperature, sea ice, or dust fluxes may also
193 play a major role in explaining changes in $p\text{CO}_2$ between the present and LGM (e.g.
194 46; 47; 2; 48). While likely to be important, these feedbacks are relatively poorly under-
195 stood and not included in our model. To address the potential role of changes in biological

196 productivity in the context of our idealized LGM experiment, we explore the upper limit
197 of biological carbon uptake by strongly increasing the maximum community production
198 rate, such that virtually all available nutrients are consumed at the surface and the model
199 approaches the maximum drawdown potential (49). In this scenario, glacial $p\text{CO}_2$ con-
200 centrations decrease to 153 ppm, surpassing the reconstructed LGM values of $\sim 180\text{-}190$
201 ppm (34). Enhanced biological productivity, therefore, provides a possible pathway for
202 a substantial CO_2 drawdown beyond the physical effects outlined here. In this experi-
203 ment, the drawdown is strongly dominated by the biological pump (Table 1) as expected.
204 By contrast, the disequilibrium pump contributes slightly negatively, because biological
205 production rapidly utilizes the excess DIC in the upwelling waters and consequently re-
206 moves the disequilibrium carbon in the mixed layer (especially around Antarctica). This
207 result shows that physical and biological effects on ocean carbon storage are not linearly
208 additive, illustrating the challenges in quantifying how different non-linearly interacting
209 mechanisms contribute to the observed lower CO_2 concentrations during the LGM.

210 The idealized simulations discussed so far do not include a seasonal cycle. While seasonally-
211 varying temperatures in this model lead to significant seasonality in the sea-ice cover
212 around Antarctica, these result in only minor differences in the stratification and circula-
213 tion (18). Here, we test the effect of adding a seasonal cycle on the carbon cycle, using an
214 additional sensitivity experiment with the same seasonal temperature forcing as in (18).
215 The seasonal cycle is found to slightly reduce CO_2 concentrations in both PI and LGM

216 simulations and since the effect is somewhat stronger in the PI simulation, the PI-LGM
217 CO₂ drawdown is slightly lower at 34 ppm (Table 1). As before, the CO₂ drawdown
218 above the solubility pump effect is dominated by the change in the disequilibrium pump,
219 although the latter is significantly weaker compared to the reference experiments without
220 seasonality, but supported (rather than compensated) by a small increase in the biological
221 pump. The difference in the decomposition of the CO₂ drawdown between the sets of sim-
222 ulations with and without seasonality primarily reflects differences in the PI simulations.
223 Specifically, the PI experiment with a seasonal cycle has a weaker biological pump but
224 stronger disequilibrium pump, likely due to differences in the details of AABW formation,
225 which affect the decomposition into biological and disequilibrium pump contributions (as
226 discussed in the context of the reference simulation above).

227 **From atmospheric cooling to increased ocean carbon storage**

228 Our results show that idealized ocean-ice-biogeochemistry simulations forced solely by
229 atmospheric cooling can not only reproduce inferred physical changes in the deep ocean
230 circulation and stratification between the pre-industrial and last glacial climate, but also
231 explain a substantial drawdown in atmospheric CO₂ concentrations. While the specific
232 numbers may need to be interpreted with caution, due to the idealized model setup, the
233 key conclusion that sea-ice dynamics and the associated circulation changes lead to an
234 increase in glacial carbon drawdown well beyond the solubility effect alone, is likely to

	CTRL	κ -50%	κ +50%	No ice	Seas. cycle	Max bio.
pCO ₂ PI	278			278	270	
pCO ₂ LGM	238	244	255	268	236	153
PI-LGM Solubility Pump	16	20	16	17	15	12
PI-LGM Biological Pump	-15	-42	-15	-16	5	122
PI-LGM Disequil. Pump	39	57	22	10	14	-10

Table 1: Atmospheric pCO₂ (ppm) in the different PI and LGM simulations discussed in this study. All experiments start from the same total carbon inventory as the PI reference simulation and have been integrated to equilibrium. The different contributions to the CO₂ drawdown between the PI and LGM simulations from the carbon pump decomposition are also shown for all simulations. For the LGM sensitivity experiments with reduced and increased vertical mixing, κ -50% and κ +50% respectively, as well as the LGM simulation with maximized biological productivity, “max bio.”, the CO₂ drawdown is computed relative to the PI CTRL simulation. The DIC distribution in the sensitivity experiments is shown and discussed further in the Supplementary Material (Figure S1).

235 be robust. The results, therefore, highlight the critical role of Antarctic sea ice in our
236 understanding of glacial-interglacial transitions and that physical changes alone, triggered
237 directly by atmospheric cooling, can provide a major contribution to the lowering of
238 glacial atmospheric CO₂ concentrations. This would be consistent with the close coupling
239 between CO₂ and Antarctic air temperatures, as observed in the ice core record (34).

240 **Methods**

241 **Ocean-sea-ice model**

242 The coupled ocean and sea-ice model configuration is the same as discussed in a previ-
243 ous manuscript (18), and uses the Massachusetts Institute of Technology ocean general
244 circulation model (MITgcm; 50) in an idealized single-basin domain extending from 70°S
245 to 65°N and covering 72° in longitude, with a re-entrant channel at the southern end
246 of the domain (representing the Southern Ocean). The ocean has a uniform depth of
247 4 km, except for a sill in the Southern Ocean, which extends the continental barrier
248 below 3 km depth. The horizontal resolution is $1^\circ \times 1^\circ$ and we use 29 vertical levels
249 with varying thicknesses from 20 m at the surface to 200 m in the deep ocean. Diapy-
250 cnal mixing is prescribed via a vertically varying profile, which is based on estimates of
251 mixing driven by breaking internal waves (51). The diffusivity values range from about
252 $2 \times 10^{-5} \text{m}^2 \text{s}^{-1}$ in the thermocline region to about $2 \times 10^{-4} \text{m}^2 \text{s}^{-1}$ in the abyss (18). Ad-
253 ditional sensitivity experiments are performed where the diapycnal diffusivity has been
254 reduced and increased by 50%. Mesoscale eddy effects are described via an eddy-driven
255 overturning streamfunction(52) and along-isopycnal diffusion (53), with a variable eddy
256 diffusivity (54). The ocean component is coupled to a dynamic viscous-plastic sea-ice
257 model (55). All atmospheric forcing fields are kept constant in time, with the exception
258 of the sensitivity experiments including a seasonal cycle, where surface air temperatures

259 vary every calendar month with the annual mean temperatures as in the other simulations
260 (18). Surface heat exchange restores the sea surface temperature to a prescribed zonally
261 symmetric atmospheric temperature and salt fluxes are computed from a fixed zonally
262 symmetric profile of evaporation-precipitation (18). A no-flux condition is applied at the
263 bottom boundary, i.e. geothermal heating is neglected. The changes in ocean circula-
264 tion observed between the PI and LGM experiments do not appear to be sensitive to the
265 details of the thermal boundary conditions (18), but additional details and sensitivity ex-
266 periments can be found in (18). Crucially, the only difference in the boundary conditions
267 between our PI and LGM simulations is a polar-amplified reduction in atmospheric tem-
268 peratures, ranging from 2°C in the tropics to about 6°C at the poles, which is consistent
269 with LGM proxy data (18, and references therein).

270 **Carbon cycle and atmosphere coupling**

271 The ocean-sea-ice component is coupled to an online biogeochemical model (32), which
272 includes cycles of dissolved inorganic carbon (DIC), alkalinity, oxygen, phosphate, and
273 dissolved organic phosphorus. Different elements are linked by fixed Redfield stoichio-
274 metric ratios of $R[\text{C:N:P:O}] = 117:16:1:-170$ in biologically-mediated transformations.
275 Phosphate and light availability regulate the rates of carbon uptake and oxygen produc-
276 tion by biological productivity, where phosphate consumption by biology is transformed
277 into dissolved organic matter and the remaining portion sinks down as particulate organic

278 matter; some fraction is not utilized and subducted as dissolved inorganic (or preformed)
279 nutrients (32). Calcium carbonate production is computed via a fixed rain ratio of 5%
280 and carbonate chemistry is solved explicitly (56). The air-sea exchange of CO₂ is param-
281 eterized with a gas transfer coefficient that depends on the square of the local wind speed
282 (57). Wind speed is computed based on the mean wind fields shown in (18), to which we
283 add a gustiness of 6.5 m s⁻¹, which leads to a global mean piston velocity of 20 cm h⁻¹
284 (e.g. 58). A different value for the gas transfer coefficient was tested, in line with more
285 recent estimates (59), but this made very little difference (not shown). In sea-ice covered
286 regions, air-sea gas exchange is reduced by a factor representing the ice-covered fraction
287 of the grid box (except for the sensitivity experiment where the effect of sea ice on air-sea
288 fluxes is removed - see Table 1).

289 The model is first integrated in the control configuration with pre-industrial boundary
290 conditions, prescribed atmospheric pCO₂ of 278 ppm, and initial values for alkalinity and
291 DIC concentrations taken from (24). The model is integrated to equilibrium and the
292 final state provides the initial conditions for all simulations discussed in the manuscript.
293 The model is then coupled to an atmospheric box, which consists of a well-mixed carbon
294 reservoir (33), such as to ensure conservation of the total amount of carbon; however,
295 atmospheric CO₂ is not radiatively-active, which means that there are no carbon cycle
296 feedbacks on the rest of the simulated climate system. The mass of the atmosphere is
297 scaled down to 4.9×10^{19} moles, so that the observed ratio between atmosphere and ocean

298 mass is approximately equal to reality. All coupled ocean-ice-atmosphere simulations are
299 again integrated to full equilibrium.

300 **Carbon pump decomposition**

301 The carbon pump is decomposed into various components with the help of explicit tracers
302 for preformed phosphate and preformed alkalinity (60). These tracers are reset to the
303 local phosphate concentration and alkalinity at the surface, while being treated as passive
304 tracers below. The alternative would be to extrapolate preformed alkalinity and phosphate
305 using apparent oxygen utilization (36; 29); this leads to different results for the carbon
306 pump decomposition (not shown) and may generate substantial overestimations and biases
307 in the interpretation (41).

308 The preformed phosphate and alkalinity tracers allow us to separate DIC in the ocean
309 into components associated with the surface saturated carbon concentration, C_{sat} , the soft
310 tissue biological pump, C_{soft} , the carbonate pump, C_{carb} , and the disequilibrium pump,
311 C_{dis} . C_{sat} can at any point be computed directly based on the temperature, salinity,
312 preformed alkalinity and atmospheric $p\text{CO}_2$ using the carbonate chemistry equations (56).
313 C_{soft} is computed as:

$$C_{soft} = 117(P - P_{pre}) \quad (1)$$

314 where P is the total Phosphate and P_{pre} the preformed Phosphate concentration. C_{carb}

315 is computed as:

$$C_{carb} = \frac{1}{2}[A_T - A_{pre} + 16(P - P_{Pre})] \quad (2)$$

316 where A_T is in-situ alkalinity and A_{pre} is preformed Alkalinity (36). Finally, C_{dis} follows
317 as:

$$C_{dis} = DIC - C_{sat} - C_{soft} - C_{carb}. \quad (3)$$

318 The separation of total DIC into C_{sat} , C_{soft} , C_{carb} , and C_{dis} for the control PI and LGM
319 simulations is shown in Figures S2, S3 (Supplementary Material). The results for the PI
320 simulation are broadly consistent with previous studies (61; 36; 37), although the compa-
321 rability to models and observations with realistic continental configuration is limited by
322 our single-basin geometry, where deep-ocean water masses share aspects with both the
323 Atlantic and the Pacific. Comparison to observations is further limited by the indirect
324 methods required to obtain the carbon pump separation from observable quantities and
325 by the disequilibrium contribution associated with anthropogenic CO₂ uptake (61).

326 To attribute the atmospheric CO₂ drawdown to components associated with the different
327 pumps, we consider the global carbon inventory (25; 35):

$$\Sigma C = MpCO_2 + V[C_{sat} + C_{dis} + C_{soft} + C_{carb}] \quad (4)$$

328 Here ΣC is the total amount of inorganic carbon in the atmosphere and ocean, M is the
329 molar volume of the atmosphere (4.9×10^{19} moles in our model) and V is the volume of

330 the ocean ($3.6 \times 10^{17} \text{m}^3$ in our model). Since the organic carbon contribution to the total
 331 carbon budget is negligible, ΣC is approximately constant, and changes in the various
 332 reservoirs between our pre-industrial and glacial simulations obey:

$$\delta pCO_2 = \frac{V}{M} [\delta C_{sat} + \delta C_{dis} + \delta C_{soft} + \delta C_{carb}] \quad (5)$$

333 Ignoring nonlinearities, we can further de-compose δC_{sat} into contributions associated with
 334 changes in temperature, δC_T , salinity, δC_S , preformed alkalinity, δC_A , and atmospheric
 335 CO_2 concentration itself, δC_{CO_2} (36):

$$\delta C_{sat} \approx \delta C_T + \delta C_S + \delta C_A + \delta C_{CO_2} \quad (6)$$

336 where:

$$\delta C_T = \frac{\partial C_{sat}}{\partial T} \delta T, \quad \delta C_S = \frac{\partial C_{sat}}{\partial S} \delta S, \quad \delta C_A = \frac{\partial C_{sat}}{\partial A} \delta A, \quad \delta C_{CO_2} = \frac{\partial C_{sat}}{\partial pCO_2} \delta pCO_2. \quad (7)$$

337 Combining Eqs. (5) and (6) and re-arranging, we obtain:

$$\delta pCO_2 = \alpha [\delta C_{sol} + \delta C_{dis} + \delta C_{bio}] \quad (8)$$

338 where $\alpha \equiv \left[M/V + \frac{\partial C_{sat}}{\partial pCO_2} \right]^{-1}$, $\delta C_{sol} = \delta C_T + \delta C_S$ denotes the total change associated
 339 with the solubility pump, which here is dominated by the temperature effect (see Table

340 S1, Supplementary Material), and $\delta C_{bio} = \delta C_{soft} + \delta C_{carb} + \delta C_A$ denotes the net effect of
 341 the biological pump. Here, changes in preformed alkalinity are driven primarily by the
 342 carbonate pump, which acts to increase the alkalinity gradient between the surface and
 343 the deep ocean. δC_A is therefore directly linked to the carbonate pump and overcompen-
 344 sates for the effect of δC_{carb} , such that a strengthening of the carbonate pump acts to
 345 raise atmospheric CO_2 concentrations (35). Since the soft tissue and carbonate pumps are
 346 tightly linked in our model, we further combine them into a net biological pump contri-
 347 bution. Changes in the biological pump are generally dominated by the soft tissue pump
 348 with the net effect of the carbonate pump ($\delta C_{carb} + \delta C_A$) partially compensating in most
 349 cases (Table S1, Supplementary Material).

350 The contributions of the solubility, disequilibrium, and biological pumps to the total
 351 atmospheric pCO_2 change between the PI and LGM simulations are then defined as:

$$(\delta p\text{CO}_2)_{sol} \equiv \alpha \delta C_{sol}, \quad (\delta p\text{CO}_2)_{dis} \equiv \alpha \delta C_{dis}, \quad (\delta p\text{CO}_2)_{bio} \equiv \alpha \delta C_{bio}, \quad (9)$$

352 where α can either be computed directly or inferred from Eq. (8) as:

$$\alpha = \frac{\delta p\text{CO}_2}{\delta C_{sol} + \delta C_{dis} + \delta C_{bio}}. \quad (10)$$

353 We here use Eq. (10), but either approximation leads to very similar results.

354 **Data Availability**

355 The input files used to run the MITgcm simulations that support the findings of this
356 study are available from the corresponding author upon request. The model output data
357 for all simulations can be obtained from: github.com/alicemarzocchi/MITgcmOutput.

358 **Code Availability**

359 The MITgcm code is freely available for download at <https://doi.org/10.5281/zenodo.1409237>.
360 Computer code used to process the model output and generate figures is available from
361 the corresponding author on request.

362 **References**

- 363 [1] Sigman, D.M. & Boyle, E.A. Glacial/interglacial variations in atmospheric carbon
364 dioxide. *Nature* **407**, 859 (2000).
- 365 [2] Brovkin, V., Ganopolski, A., Archer, D. & Rahmstorf, S. Lowering
366 of glacial atmospheric CO₂ in response to changes in oceanic circulation
367 and marine biogeochemistry. *Paleoceanography* **22**, PA4202 (2007). URL
368 <http://onlinelibrary.wiley.com/doi/10.1029/2006PA001380/abstract>.
- 369 [3] Marshall, J. & Speer, K. Closure of the meridional overturning circulation

- 370 through Southern Ocean upwelling. *Nature Geoscience* **5**, 171–180 (2012). URL
371 <http://www.nature.com/ngeo/journal/v5/n3/abs/ngeo1391.html>.
- 372 [4] Marchitto, T.M., Oppo, D.W. & Curry, W.B. Paired benthic foraminiferal cd/ca
373 and zn/ca evidence for a greatly increased presence of southern ocean water in the
374 glacial north atlantic. *Paleoceanography* **17**, 10–1 (2002).
- 375 [5] Curry, W.B. & Oppo, D.W. Glacial water mass geometry and the distribution of
376 $\delta^{13}\text{C}$ of $\sum\text{CO}_2$ in the western Atlantic Ocean. *Paleoceanogr.* **20**, PA1017 (2005).
- 377 [6] Lippold, J. *et al.* Strength and geometry of the glacial atlantic meridional overturning
378 circulation. *Nature Geoscience* **5**, 813 (2012).
- 379 [7] Adkins, J.F., McIntyre, K. & Schrag, D.P. The Salinity, Temperature, and
380 $\delta^{18}\text{o}$ of the Glacial Deep Ocean. *Science* **298**, 1769–1773 (2002). URL
381 <http://science.sciencemag.org/content/298/5599/1769>.
- 382 [8] Insua, T.L., Spivack, A.J., Graham, D., D'Hondt, S. & Moran, K. Reconstruction
383 of pacific ocean bottom water salinity during the last glacial maximum. *Geophysical*
384 *Research Letters* **41**, 2914–2920 (2014).
- 385 [9] Wunsch, C. Pore fluids and the {LGM} ocean salinity reconsid-
386 ered. *Quaternary Science Reviews* **135**, 154 – 170 (2016). URL
387 <http://www.sciencedirect.com/science/article/pii/S0277379116300178>.

- 388 [10] Otto-Bliesner, B.L. *et al.* Last Glacial Maximum ocean thermo-
389 haline circulation: PMIP2 model intercomparisons and data con-
390 straints. *Geophysical Research Letters* **34**, L12706 (2007). URL
391 <http://onlinelibrary.wiley.com/doi/10.1029/2007GL029475/abstract>.
- 392 [11] Muglia, J. & Schmittner, A. Glacial Atlantic overturning increased by wind stress
393 in climate models. *Geophysical Research Letters* **42**, 2015GL064583 (2015). URL
394 <http://onlinelibrary.wiley.com/doi/10.1002/2015GL064583/abstract>.
- 395 [12] Marzocchi, A. & Jansen, M.F. Connecting antarctic sea ice to deep-ocean circulation
396 in modern and glacial climate simulations. *Geophysical Research Letters* **44**, 6286–
397 6295 (2017).
- 398 [13] Stephens, B.B. & Keeling, R.F. The influence of Antarctic sea ice on
399 glacial–interglacial CO₂ variations. *Nature* **404**, 171–174 (2000). URL
400 <http://www.nature.com/nature/journal/v404/n6774/abs/404171a0.html>.
- 401 [14] Shin, S.-I. *et al.* A Simulation of the Last Glacial Maximum climate
402 using the NCAR-CCSM. *Climate Dynamics* **20**, 127–151 (2003). URL
403 <http://link.springer.com/article/10.1007/s00382-002-0260-x>.
- 404 [15] Bouttes, N., Paillard, D. & Roche, D.M. Impact of brine-induced stratifi-
405 cation on the glacial carbon cycle. *Clim. Past* **6**, 575–589 (2010). URL
406 <http://www.clim-past.net/6/575/2010/>.

- 407 [16] Watson, A.J. & Naveira Garabato, A.C. The role of southern ocean mixing and
408 upwelling in glacial-interglacial atmospheric co2 change. *Tellus B: Chemical and*
409 *Physical Meteorology* **58**, 73–87 (2006).
- 410 [17] Ferrari, R. *et al.* Antarctic sea ice control on ocean circulation in present and glacial
411 climates. *Proceedings of the National Academy of Sciences* **111**, 8753–8758 (2014).
412 URL <http://www.pnas.org/content/111/24/8753>.
- 413 [18] Jansen, M.F. Glacial ocean circulation and stratification explained by reduced atmo-
414 spheric temperature. *Proceedings of the National Academy of Sciences* **114**, 45–50
415 (2017). URL <http://www.pnas.org/content/114/1/45>.
- 416 [19] Sun, S., Eisenman, I. & Stewart, A.L. The influence of Southern Ocean sur-
417 face buoyancy forcing on glacial-interglacial changes in the global deep ocean
418 stratification. *Geophysical Research Letters* **43**, 2016GL070058 (2016). URL
419 <http://onlinelibrary.wiley.com/doi/10.1002/2016GL070058/abstract>.
- 420 [20] Galbraith, E. & de Lavergne, C. Response of a comprehensive climate model to
421 a broad range of external forcings: Relevance for deep ocean ventilation and the
422 development of late Cenozoic ice ages. *Climate Dynamics* **52**, 653–679 (2019).
- 423 [21] Nadeau, L.-P., Ferrari, R. & Jansen, M.F. Antarctic sea ice control on the depth of
424 North Atlantic Deep Water. *Journal of Climate* **32**, 2537–2551 (2019).
- 425 [22] Jansen, M.F. & Nadeau, L.-P. The Effect of Southern Ocean Sur-

- 426 face Buoyancy Loss on the Deep-Ocean Circulation and Stratifica-
427 tion. *Journal of Physical Oceanography* **46**, 3455–3470 (2016). URL
428 <http://journals.ametsoc.org/doi/abs/10.1175/JPO-D-16-0084.1>.
- 429 [23] Sarmiento, J.L. & Toggweiler, J. A new model for the role of the oceans in deter-
430 mining atmospheric pco2. *Nature* **308**, 621 (1984).
- 431 [24] Archer, D.E. *et al.* Atmospheric pco2 sensitivity to the biological pump in the ocean.
432 *Global Biogeochemical Cycles* **14**, 1219–1230 (2000).
- 433 [25] Ito, T. & Follows, M.J. Preformed phosphate, soft tissue pump and atmospheric co2.
434 *Journal of Marine Research* **63**, 813–839 (2005).
- 435 [26] Kohfeld, K.E. & Ridgwell, A. Glacial-interglacial variability in atmospheric co2.
436 *Surface ocean-lower atmosphere processes* **187**, 251–286 (2009).
- 437 [27] Watson, A.J., Vallis, G.K. & Nikurashin, M. Southern Ocean buoyancy forcing of
438 ocean ventilation and glacial atmospheric CO2. *Nature Geoscience* **8**, 861–864 (2015).
439 URL <http://www.nature.com/ngeo/journal/v8/n11/abs/ngeo2538.html>.
- 440 [28] Ganopolski, A. & Brovkin, V. Simulation of climate, ice sheets and co2 evolution
441 during the last four glacial cycles with an earth system model of intermediate com-
442 plexity. *Climate of the Past* **13**, 1695–1716 (2017).
- 443 [29] Ferreira, D., Marshall, J., Ito, T. & McGee, D. Linking glacial-interglacial states to
444 multiple equilibria of climate. *Geophysical Research Letters* **45**, 9160–9170 (2018).

- 445 [30] Gersonde, R., Crosta, X., Abelmann, A. & Armand, L. Sea-surface tem-
446 perature and sea ice distribution of the Southern Ocean at the EPILOG
447 Last Glacial Maximum—a circum-Antarctic view based on siliceous micro-
448 fossil records. *Quaternary Science Reviews* **24**, 869–896 (2005). URL
449 <http://www.sciencedirect.com/science/article/pii/S0277379104002227>.
- 450 [31] Lund, D., Adkins, J. & Ferrari, R. Abyssal atlantic circulation during the last
451 glacial maximum: Constraining the ratio between transport and vertical mixing.
452 *Paleoceanography* **26** (2011).
- 453 [32] Dutkiewicz, S., Follows, M.J. & Parekh, P. Interactions of the iron and phosphorus
454 cycles: A three-dimensional model study. *Global Biogeochemical Cycles* **19** (2005).
- 455 [33] Parekh, P., Follows, M.J., Dutkiewicz, S. & Ito, T. Physical and biological regulation
456 of the soft tissue carbon pump. *Paleoceanography and Paleoclimatology* **21** (2006).
- 457 [34] Petit, J.-R. *et al.* Climate and atmospheric history of the past 420,000 years from
458 the vostok ice core, antarctica. *Nature* **399**, 429 (1999).
- 459 [35] Goodwin, P., Follows, M.J. & Williams, R.G. Analytical relationships between atmo-
460 spheric carbon dioxide, carbon emissions, and ocean processes. *Global Biogeochemical*
461 *Cycles* **22** (2008).
- 462 [36] Lauderdale, J.M., Garabato, A. C.N., Oliver, K.I., Follows, M.J. & Williams, R.G.

- 463 Wind-driven changes in southern ocean residual circulation, ocean carbon reservoirs
464 and atmospheric CO_2 . *Climate dynamics* **41**, 2145–2164 (2013).
- 465 [37] Munday, D., Johnson, H. & Marshall, D. Impacts and effects of mesoscale ocean
466 eddies on ocean carbon storage and atmospheric pCO_2 . *Global Biogeochemical Cycles*
467 **28**, 877–896 (2014).
- 468 [38] Follows, M.J., Ito, T. & Marotzke, J. The wind-driven, subtropical gyres and the
469 solubility pump of CO_2 . *Global biogeochemical cycles* **16** (2002).
- 470 [39] Toggweiler, J., Gnanadesikan, A., Carson, S., Murnane, R. & Sarmiento, J. Repre-
471 sentation of the carbon cycle in box models and GCMs: 1. solubility pump. *Global*
472 *Biogeochemical Cycles* **17** (2003).
- 473 [40] Foster, T.D. An analysis of the cabbeling instability in sea water. *Journal of Physical*
474 *Oceanography* **2**, 294–301 (1972).
- 475 [41] Khatiwala, S., Schmittner, A. & Muglia, J. Air-sea disequilibrium enhances ocean
476 carbon storage during glacial periods. *Science advances* **5**, eaaw4981 (2019).
- 477 [42] Green, J. *et al.* Tidal mixing and the meridional overturning circulation from the
478 Last Glacial Maximum. *Geophysical Research Letters* **36** (2009).
- 479 [43] Schmittner, A., Green, J. & Wilmes, S.-B. Glacial ocean overturning intensified by
480 tidal mixing in a global circulation model. *Geophysical Research Letters* **42**, 4014–
481 4022 (2015).

- 482 [44] Wunsch, C. & Ferrari, R. Vertical mixing, energy, and the general circulation of the
483 oceans. *Annu. Rev. Fluid Mech.* **36**, 281–314 (2004).
- 484 [45] Marinov, I. *et al.* Impact of oceanic circulation on biological carbon storage in the
485 ocean and atmospheric pco₂. *Global Biogeochemical Cycles* **22** (2008).
- 486 [46] Mix, A.C. Influence of productivity variations on long-term atmospheric CO₂. *Nature*
487 **337**, 541 (1989).
- 488 [47] Kohfeld, K.E., Le Quéré, C., Harrison, S.P. & Anderson, R.F. Role of marine biology
489 in glacial-interglacial co₂ cycles. *Science* **308**, 74–78 (2005).
- 490 [48] Martínez-García, A. *et al.* Iron fertilization of the subantarctic ocean during the last
491 ice age. *Science* **343**, 1347–1350 (2014).
- 492 [49] Ödalen, M., Nycander, J., Oliver, K.I., Brodeau, L. & Ridgwell, A. The influence of
493 the ocean circulation state on ocean carbon storage and co₂ drawdown potential in
494 an earth system model. *Biogeosciences* **15**, 1367–1393 (2018).
- 495 [50] Marshall, J., Hill, C., Perelman, L. & Adcroft, A. Hydrostatic, quasi-hydrostatic,
496 and nonhydrostatic ocean modeling. *Journal of Geophysical Research: Oceans* **102**,
497 5733–5752 (1997).
- 498 [51] Nikurashin, M. & Ferrari, R. Overturning circulation driven by breaking internal
499 waves in the deep ocean. *Geophys. Res. Lett.* **40**, 3133–3137 (2013).

- 500 [52] Gent, P.R. & McWilliams, J.C. Isopycnal mixing in ocean circulation models. *J.*
501 *Phys. Oceanogr.* **20**, 150–155 (1990).
- 502 [53] Redi, M. Oceanic isopycnal mixing by coordinate rotation. *J. Phys. Oceanogr.* **12**,
503 1154–1158 (1982).
- 504 [54] Visbeck, M., Marshall, J., Haine, T. & Spall, M. Specification of eddy transfer
505 coefficients in coarse-resolution ocean circulation models. *J. Phys. Oceanogr.* **27**,
506 381–402 (1997).
- 507 [55] Losch, M., Menemenlis, D., Campin, J.-M., Heimbach, P. & Hill, C. On the for-
508 mulation of sea-ice models. part 1: Effects of different solver implementations and
509 parameterizations. *Ocean Modelling* **33**, 129–144 (2010).
- 510 [56] Follows, M.J., Ito, T. & Dutkiewicz, S. On the solution of the carbonate chemistry
511 system in ocean biogeochemistry models. *Ocean Modelling* **12**, 290–301 (2006).
- 512 [57] Wanninkhof, R. Relationship between wind speed and gas exchange over the ocean.
513 *Journal of Geophysical Research: Oceans* **97**, 7373–7382 (1992).
- 514 [58] Krakauer, N.Y., Randerson, J.T., Primeau, F.W., Gruber, N. & Menemenlis, D.
515 Carbon isotope evidence for the latitudinal distribution and wind speed dependence
516 of the air–sea gas transfer velocity. *Tellus B: Chemical and Physical Meteorology* **58**,
517 390–417 (2006).

518 [59] Wanninkhof, R. Relationship between wind speed and gas exchange over the ocean
519 revisited. *Limnology and Oceanography: Methods* **12**, 351–362 (2014).

520 [60] Ito, T. & Follows, M.J. Air-sea disequilibrium of carbon dioxide enhances the biolog-
521 ical carbon sequestration in the southern ocean. *Global Biogeochemical Cycles* **27**,
522 1129–1138 (2013).

523 [61] Williams, R.G. & Follows, M.J. *Ocean dynamics and the carbon cycle: Principles*
524 *and mechanisms* (Cambridge University Press, 2011).

525 **Acknowledgments**

526 This work was funded by the National Science Foundation under Awards OCE-1536454
527 and OCE-1846821 and computational resources were provided by the Research Com-
528 puting Center at the University of Chicago. AM received funding from NERC grant
529 NE/P019293/1 (TICTOC).

530 **Author contributions**

531 AM and MFJ designed the study. AM performed the numerical simulations and analyzed
532 the results. AM and MFJ interpreted the results and wrote the manuscript.

533 **Corresponding author**

534 Correspondence to Alice Marzocchi (alice.marzocchi@noc.ac.uk) .

535 **Competing interests**

536 The authors declare no competing interests.

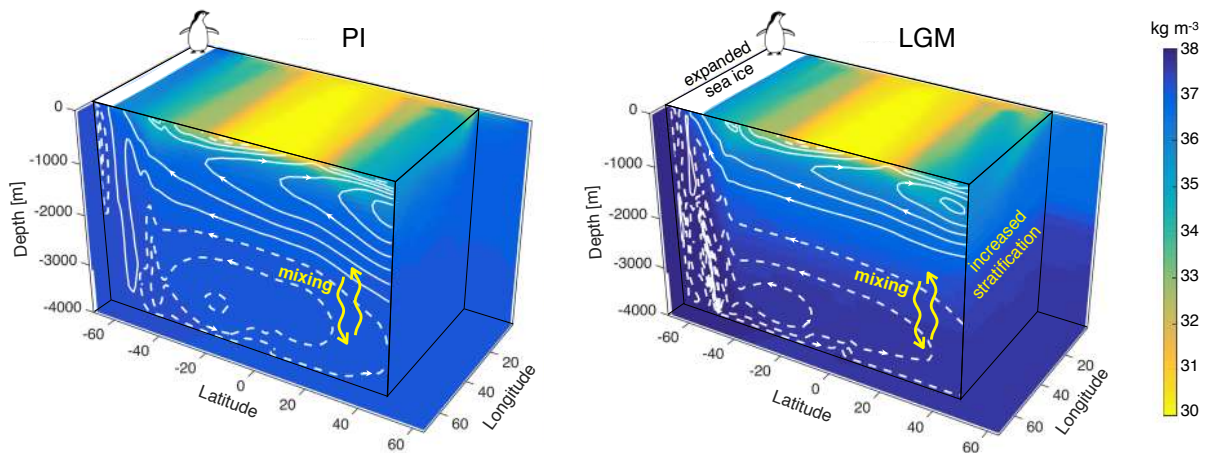


Figure 1: Changes in ocean circulation and sea ice cover between the preindustrial (PI) and Last Glacial Maximum (LGM). Figures show potential density referenced to 2000 m (shading) and meridional overturning streamfunction (contours; solid lines for positive values and dashed for negative ones) for the PI and LGM reference simulations. Note that 1000 kg m^{-3} has been subtracted from the potential density values. Sea ice cover of 25% or more is shown at the southern end of the domain (top face).

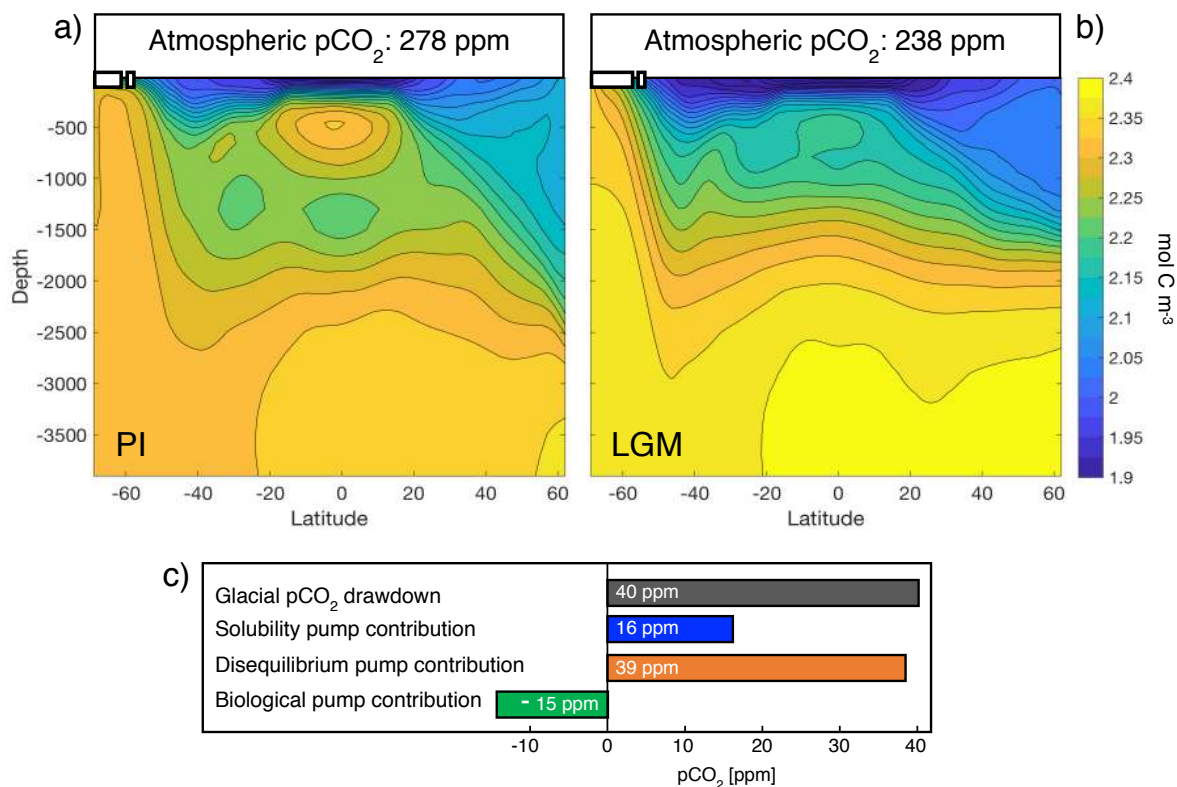


Figure 2: Deep ocean carbon storage and atmospheric CO_2 concentrations in the PI and LGM reference simulations. Figures show zonally averaged dissolved inorganic carbon (DIC) and atmospheric CO_2 concentration; Antarctic sea-ice cover is sketched in white (a,b). The breakdown of the overall LGM $p\text{CO}_2$ change into different ocean carbon storage terms is shown for the reference simulation (c). The biological pump term includes contributions from both soft tissue and carbonate pumps, and the alkalinity effect of the latter (see Methods for more details). The distribution of the four components is shown and discussed further in the Supplementary Material (Figures S2 and S3).